AGU PUBLICATIONS

JGR

Journal of Geophysical Research: Oceans

RESEARCH ARTICLE
10.1002/2015JC011573

Special Section:
Physical Processes Responsible for Material Transport in the Gulf of Mexico for Oil Spill Applications

Quantifying uncertainty in Gulf of Mexico forecasts stemming from uncertain initial conditions

Mohamed Iskandarani[1], Matthieu Le Hénaff[2,3], William Carlisle Thacker, Ashwanth Srinivasan[4], and Omar M. Knio[5,6]

[1]Rosenstiel School of Marine and Atmospheric Science, University of Miami, Miami, Florida, USA, [2]CIMAS, University of Miami, Miami, Florida, USA, [3]AOML, NOAA, Miami, Florida, USA, [4]Tendral LLC, Miami, Florida, USA, [5]Department of Mechanical Engineering & Materials Science, Duke University, Durham, North Carolina, USA, [6]Division of Computer, Electrical and Mathematical Science and Engineering, King Abdullah University of Science and Technology, Thuwal, Saudi Arabia

Abstract Polynomial Chaos (PC) methods are used to quantify the impacts of initial conditions uncertainties on oceanic forecasts of the Gulf of Mexico circulation. Empirical Orthogonal Functions are used as initial conditions perturbations with their modal amplitudes considered as uniformly distributed uncertain random variables. These perturbations impact primarily the Loop Current system and several frontal eddies located in its vicinity. A small ensemble is used to sample the space of the modal amplitudes and to construct a surrogate for the evolution of the model predictions via a nonintrusive Galerkin projection. The analysis of the surrogate yields verification measures for the surrogate's reliability and statistical information for the model output. A variance analysis indicates that the sea surface height predictability in the vicinity of the Loop Current is limited to about 20 days.

Key Points:
- Polynomial Chaos were used to quantify uncertainties in oceanic forecasts caused by initial conditions uncertainties
- Uncertainty in the strength of a frontal eddy controls uncertainty in the forecast
- Variance analysis suggests a loss of predictability in SSH in the Loop Current pinch-off region after day 20

Correspondence to:
M. Iskandarani,
miskandarani@rsmas.miami.edu

Citation:
Iskandarani, M., M. Le Hénaff, W. C. Thacker, A. Srinivasan, and O. M. Knio (2016), Quantifying uncertainty in Gulf of Mexico forecasts stemming from uncertain initial conditions, *J. Geophys. Res. Oceans*, *121*, 4819–4832, doi:10.1002/2015JC011573.

Received 15 DEC 2015
Accepted 5 JUN 2016
Accepted article online 9 JUN 2016
Published online 16 JUL 2016

1. Introduction

Material transport in the surface ocean is controlled by the combined action of ocean currents, waves and winds [*Reed et al*., 1999; *Le Hénaff et al*., 2012; *Curcic et al*., 2016]. Modeling material transport, for either risk management or for planning a response to an accidental oil spill, requires oceanic and atmospheric forecasts. The accuracy and usefulness of the transport model thus depends critically on the quality of these forecasts. Unfortunately, atmospheric and oceanic forecasts are inherently uncertain because of uncertainties in the models, and because of uncertainties in their input data such as the model's initial and boundary conditions, forcing, empirical parameters in subgrid scale models, etc. Useful forecasts should thus include, in addition to the most likely estimates of the environmental conditions, a quantitative assessment of the uncertainties in these forecasts. Policy makers and emergency response managers are then able to consider a range of scenarios and outcomes that reflect the uncertainties in the environmental conditions.

The present article explores the use of Polynomial Chaos (PC) techniques [*Ghanem and Spanos*, 2003; *Najm*, 2009; *Le Maître and Knio*, 2010] to quantify the uncertainties in a HYCOM [*Bleck*, 2002] forecast of the circulation in the Gulf of Mexico stemming from uncertainties in the model's initial conditions. The study period extends from 1 May 2010 until 30 June 2010 when the major concern was whether the oil spilled during the Deep Water Horizon accident would be entrained in the Loop Current. This period coincides with the presence of a frontal cyclone that influenced the shedding of Loop Current Eddy Franklin [*Kantha*, 2014]. The focus of the present article is thus on quantifying the uncertainties in the HYCOM forecast given the uncertainty in the strength and position of the frontal cyclone.

The major distinguishing feature of PC methods is the establishment of a functional relationship between the uncertain input data and the uncertain output. This functional relationship takes the form of a spectral series:

$$M(\boldsymbol{x},t,\boldsymbol{\xi}) \approx M_P(\boldsymbol{x},t,\boldsymbol{\xi}) = \sum_{n=0}^{P} \widehat{M}_n(\boldsymbol{x},t)\,\Psi_n(\boldsymbol{\xi}) \tag{1}$$

where $M(\boldsymbol{x},t,\boldsymbol{\xi})$ is a model output that depends on space $\boldsymbol{x}$, time t and the uncertain input variables $\boldsymbol{\xi}$, M_P is the series representation of the model output, $\widehat{M}_n(\boldsymbol{x},t)$ are the series coefficients, and the $\Psi_n(\boldsymbol{\xi})$ are suitably

chosen basis functions. Different flavors of polynomial chaos methods can be derived depending on the choice of basis functions, and on the method used to determine the coefficients; an overview of these different techniques is presented in *Iskandarani et al.* [2016]. Here we rely on the Galerkin projection approach [*Le Maître and Knio*, 2010; *Iskandarani et al.*, 2016]: the basis functions are orthogonal polynomials with respect to the probability density function (pdf) $\rho(\boldsymbol{\xi})$ of the uncertain variable:

$$\langle \Psi_m, \Psi_n \rangle = \int \Psi_m(\boldsymbol{\xi})\, \Psi_n(\boldsymbol{\xi})\, \rho(\boldsymbol{\xi})\, \mathrm{d}\boldsymbol{\xi} = \delta_{m,n} ||\Psi_m||^2; \tag{2}$$

and the series coefficients are determined by Galerkin projection with the integrals evaluated using numerical quadrature:

$$\widehat{M}_n(\mathbf{x}, t) = \frac{\langle M, \Psi_n \rangle}{||\Psi_n||^2} \approx \frac{\langle M, \Psi_n \rangle_Q}{||\Psi_n||^2} = \frac{1}{||\Psi_n||^2} \sum_{q=1}^{Q} M(\mathbf{x}, t, \xi_q)\omega_q. \tag{3}$$

The ξ_q and ω_q refer to multidimensional quadrature roots and weights such as tensorized Gauss quadrature. The evaluation of $M(\boldsymbol{x}, t, \xi_q)$ in equation (3) requires a model run with the uncertain variables set to specified values.

A PC series thus approximates the response of the model to changes in the uncertain variables $\boldsymbol{\xi}$. The series can be used as a faithful surrogate for the model once the coefficients $\widehat{M}_k$ are known, and forms the basis for the statistical analysis of the model output. The orthogonality of the basis with respect to the probability density function of the input allows the statistical moments of M to be calculated easily: the mean is simply the zero-th coefficient and the variance can be obtained by a weighed sum of the squared coefficients. Furthermore, the approximation properties of spectral series are well-understood: high accuracy can be achieved with few terms when M varies smoothly with $\boldsymbol{\xi}$, whereas the convergence is suboptimal when M exhibits large localized variations in the uncertainty space. The accuracy of the series can be monitored simply by inspecting the decay of the highest degree coefficients: power at the high end of the spectrum is indicative of low accuracy and missing variance.

PC methods for Uncertainty Quantification (UQ) present several advantages as their formulation combines probabilistic and approximation paradigms. The PC approach relies on a suitably chosen small ensemble to construct a model surrogate which is then leveraged to produce a much larger ensemble. This surrogate is actually a series that can be readily analyzed, for example, to determine the sensitivity of the output to particular inputs, to perform parameter estimation [*Sraj et al.*, 2014], and to calculate all the statistical moments desired analytically (thus it is akin to taking an infinite sample size). The statistical estimates are hence more *reliable* once the surrogate has been validated. The surrogate's approximation error can in fact be monitored to ascertain whether enough sampling has been performed to gain confidence in the results. PC methods have been documented [*Le Maître et al.*, 2002; *Xiu and Hesthaven*, 2005; *Nobile and Webster*, 2008; *Le Maître and Knio*, 2010; *Iskandarani et al.*, 2016] to be more efficient than Monte Carlo based methods when the dimensionality of the problem is relatively low. The primary reason for this efficiency is that the error in Monte Carlo sampling decreases only as the square root of the number of samples and accurate statistical estimates require a large sample set; this is impractical when the model is costly as is the case for an ocean circulation model. Drawing samples from a series-based surrogate, on the other hand, is much more efficient once the series coefficients are computed from a much smaller ensemble. PC methods can be implemented nonintrusively and in an ensemble fashion so that no modification of the forward model is needed. Finally, the PC approach does not impose restrictions on the output statistics or on the linearity of the forward model. It does, however, require the user to specify a distribution for the input uncertainties (the weight function appearing in the inner product 2) even though these pdfs are generally not well-known from observations; users must exercise judgement and use sensible distributions. It is worth noting that most traditional UQ in ocean and atmospheric models assume a representation for the output statistics (commonly Gaussian distributions), and are not really concerned with representing the response surface itself (the problem of specifying the input uncertainty pdf is common to all UQ approaches whether based on PC or not).

The functional nature of PC methods requires the association of an input uncertainty with a continuous random variable. This is easy enough to do with scalar quantities, but is more complicated for field quantities

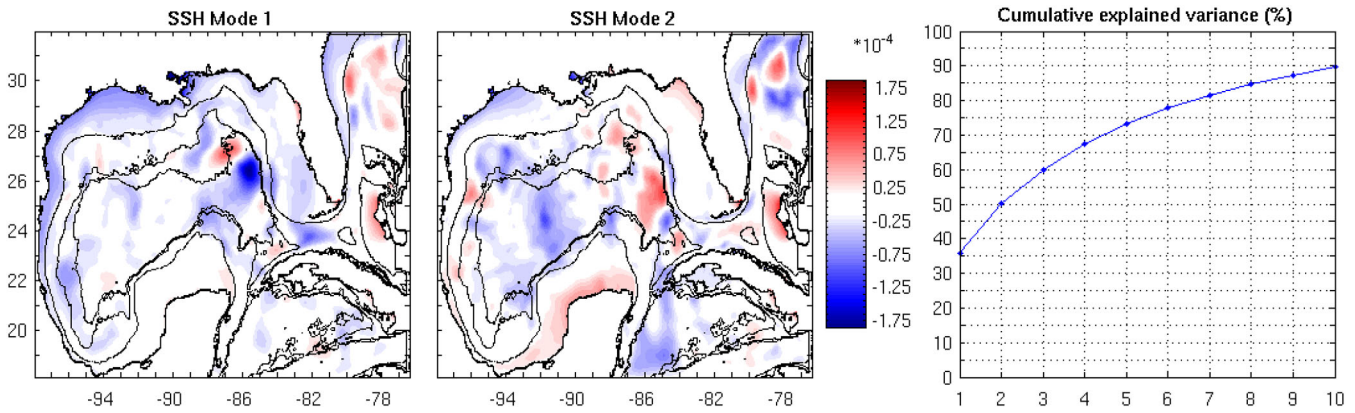

Figure 1. SSH patterns for mode 1 and 2 perturbations (left and middle) along with the cumulative variance explained by the first 10 modes.

such as the model's initial conditions. The initial conditions consist of the model state vector whose components can conceivably be varied independently. This would represent an uncertainty space with dimension in the millions for high resolution models; its exploration via quadrature sampling is computationally intractable and alternative approaches are required.

The state vector components are actually inter-dependent and are linked by various dynamical relationships and constraints. This inter-dependency allows us to identify field uncertainties with variability modes. The uncertainties can then be decomposed into modes and the components of the uncertain variables ξ can be associated with the amplitude of these modes. Furthermore, the Karahunen-Loève decomposition theorem provides the theoretical underpinnings for this modal decomposition; its discrete counterpart is the Empirical Orthogonal Function (EOF) decomposition. The modal decomposition provides a reasonable and practical pathway to "compress" uncertainties in a field to a few random variables.

In the following sections, we illustrate the application of the PC approach to quantify the uncertainties in the HYCOM forecast caused by uncertainties in the initial conditions. We focus primarily on the implementation of the uncertainty analysis and refer the reader to *Iskandarani et al*. [2016] for the description of the PC methodology. Section 2 describes the construction of EOF perturbations designed to target uncertainties associated with Loop Current frontal dynamics; it also describes the PC-ensemble used to compute the series coefficients. Section 3 presents the results of the forward propagation of the model uncertainty, and verifies the validity of the PC surrogate for various model outputs as they evolve in time. We conclude with a summary and a discussion section.

2. EOF Analysis and PC Perturbations

Our interest is focused primarily on uncertainties associated with the Loop Current (LC) and Loop Current Eddies (LCE) for short time-scale forecasts (2–3 weeks). The variability modes were thus obtained from a multivariate EOF analysis of a 14 day, data-assimilating HYCOM [*Chassignet et al*., 2007] time series. This relatively short series maximizes the probability of picking up spatially and temporally localized perturbations to the HYCOM initial conditions that can be associated with the dominant dynamical features in the basin, namely the Loop Current and its frontal eddies [*Oey et al*., 2005; *Leben*, 2005]. Furthermore the small time window minimized the interference of basin-wide modes that could have leaked into the EOF analysis had a longer series been used. Figure 1 shows the SSH spatial patterns of the first two EOF modes. The first EOF mode is localized in the Loop Current region and seems to be associated with the presence of a frontal eddy. The second mode also has a signature in the same region and can be associated with variability emanating from a Loop Current Eddy (southwest of the Loop Current region). The first and second modes explain 35% and 15% of the variance, respectively. Figure 2 shows a vertical slice of the temperature perturbation 1 day after the start of the simulation. The perturbation exhibits a temperature anomaly of -2.5°C in the vicinity of the cyclone which extends to about 400 m depth. A separate warm anomaly on the western edge of the loop current at 100m can also be discerned. Again, these anomalies seem to be localized in space and reflective of perturbations to Loop Current dynamics.

The two dominant EOF modes identified above were multiplied by two independent stochastic variables, ξ_1 and ξ_2, and added to the mean fields to perturb the initial conditions. For example, the initial layer thicknesses are given by:

$$\delta p(\boldsymbol{x}, 0, \xi_1, \xi_2) = \delta p^{(0)} + \alpha\left[\xi_1\sqrt{\lambda_1}\delta p^{(1)} + \xi_2\sqrt{\lambda_2}\delta p^{(2)}\right] \tag{4}$$

where $\delta p^{(i)}$ and λ_i refer to the i-th EOF mode and corresponding eigenvalue for $i > 0$, and for $i = 0$ refers to the unperturbed layer thickness; α is a multiplicative factor introduced to control the size of the "kick" to the initial conditions (and set to 1 for the experiments shown in the following sections). The advantages of the EOF analysis is that it compresses and ranks the input uncertainties using statistically uncorrelated modes of variability. The main disadvantage is that the EOF analysis does not focus on physical processes, as multiple processes can contribute to each mode. Note that the identification of relevant perturbation modes is a challenge shared by all ensemble based methods. It is given even more prominence within the PC paradigm because of the explicit construction of a surrogate linking input and output uncertainties, and because practicality demands a low-dimensional uncertain space.

The uncertain input variable consists of the two-dimensional vector $\boldsymbol{\xi} = (\xi_1, \xi_2)^\top$. Additional variability modes could be added but at the expense of increasing the dimension of the uncertain parameter space, and of the number of realizations needed to determine the PC coefficients (the ensemble size grows exponentially with the number of dimensions when using tensorized Gauss quadrature [*Le Maître and Knio*, 2010]). Here we limit ourselves to 2 modes to keep the computational load small for this exploratory study. This amounts to truncating the contributions of higher order modes which, with their smaller variance, can be expected to make a smaller addition to the uncertainty in the forecast compared to the dominant first two modes. The forecast uncertainty estimates presented herein can thus be considered as lower bounds of the full forecast uncertainty; the impact of including higher modes as well as additional sources of uncertainty will be reported in a future article.

The uncertain modal amplitude are assumed to be uniformly distributed in the range $|\xi_i| \leq 1$; thus $\rho(\xi_1, \xi_2) = \left(\frac{1}{2}\right)^2$. The basis functions are products of Legendre polynomials $\Psi_k(\boldsymbol{\xi}) = P_m(\xi_1)P_n(\xi_2)$ [*Le Maître and Knio*, 2010]. The highest polynomial order is set to 6 and the series is truncated in a triangular fashion so that max $(m+n) \leq 6$ as shown in Figure 3 (right); a total of 28 coefficients needed to be determined. The integrals of the Galerkin projection in equation (3) are evaluated with tensorized Gauss-Legendre quadrature rules using 7 quadrature points along each dimension (see Appendix A for more details); they hence require a total of 49 realizations. The location of the quadrature roots in the uncertainty space is shown in Figure 3; notice that these roots cluster near the edges of the interval to maximize the accuracy of the approximation and integration.

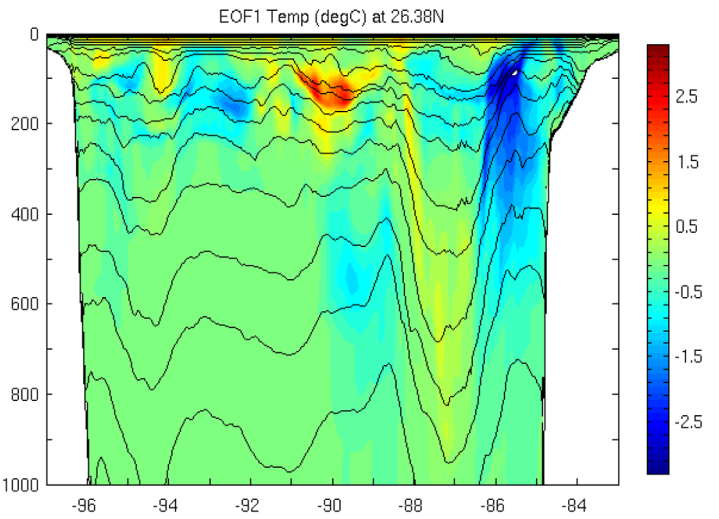

Figure 2. Vertical slice along 26.4N showing the temperature perturbations 1 day after the start of the simulation. The first mode shows a strong 2.5°C cooling in the vicinity of the frontal cyclones. The warm perturbation around 90W is at the southern edge of a small anticyclone NW of the LC.

We close this section by noting the following concerning the surrogate construction. The surrogate series serves two distinct but related purposes: it provides an accurate and efficient representation for the model response to changes in the uncertain inputs, and serves as a convenient basis for the statistical analysis of the model output. The choice of basis functions need not be tied to the specified input probability density function ρ and can be modified according to the problem requirements, for

example, to capture a particular behavior of the response surface. Some implementations of PC methods forgo the orthogonality of the series completely and opt to use interpolation or least-squares type methods; we refer the reader to the articles *Thacker et al.* [2015]; *Iskandarani et al.* [2016] for more discussion on these issues. Another benefit of PC methods is the ability to perform analysis in the uncertain space: statistical moments can be computed by integration of the basis functions, and gradients by differentiation; for example:

$$E[M] = \int \rho(\xi)\Psi_n(\xi)\,\mathrm{d}\xi \approx \sum_{n=0}^{P} \widehat{M}_n \int \rho(\xi)\Psi_n(\xi)\mathrm{d}\xi \tag{5}$$

$$\frac{\partial M}{\partial \xi} \approx \sum_{n=0}^{P} \widehat{M}_n \frac{\partial \Psi_n}{\partial \xi} \tag{6}$$

where the operator $E[]$ denotes expectation. Note that the mean estimated via equation (5) is not the same as the algebraic mean of the relatively small quadrature ensemble. The orthogonality of the basis function with respect to the input PDF simplifies the calculations of the statistical moments, and allows the use of a relatively low order expansion to represent the uncertainty in the model data accurately. Recently, *Sapsis and Lermusiaux* [2009] and *Ueckermann et al.* [2013] presented an algorithm to evolve the basis functions dynamically to maintain orthogonality as the model PDF evolves. Here in our nonintrusive ensemble approach, the basis functions are kept fixed as their optimality is not the focus of the present article.

3. Uncertainty Analysis

The HYCOM configuration used to produce the PC quadrature ensemble is the US Navy operational configuration with its 1/25° horizontal resolution and 20 vertical levels. The computational domain is open along portions of its southern, eastern and northern boundaries, where values are provided by a lower-resolution 1/12° HYCOM configured for the Atlantic Ocean [*Chassignet et al.*, 2007]. The model is forced at the surface by 3 hourly outputs from the Coupled Ocean/Atmosphere Mesoscale Prediction System (COAMP) [*Hodur*, 1997], which has 27 km resolution. The output of the 49 HYCOM ensemble was saved daily and the uncertainty analysis is performed as a postprocessing operation. Although the uncertainty analysis can be performed on any model output desired, here we focus on analysing the uncertainties in Sea Surface Height (SSH) and on temperature along a vertical section at 25° N. This analysis consists of establishing the validity of the PC surrogates, and on calculating the mean and standard deviation of SSH and temperature.

3.1. The Quadrature Ensemble

Figure 4 shows the SSH evolution for the circled samples in Figure 3, as well as the ensemble mean. The SSH contours support the association of the perturbations with the frontal eddy's strength on day 1, where it is clearly suppressed in the negative perturbations (1,1) and strengthened in the positive perturbation (7,7). An eddy shedding event is recorded for all three realizations but with different timings: the shedding

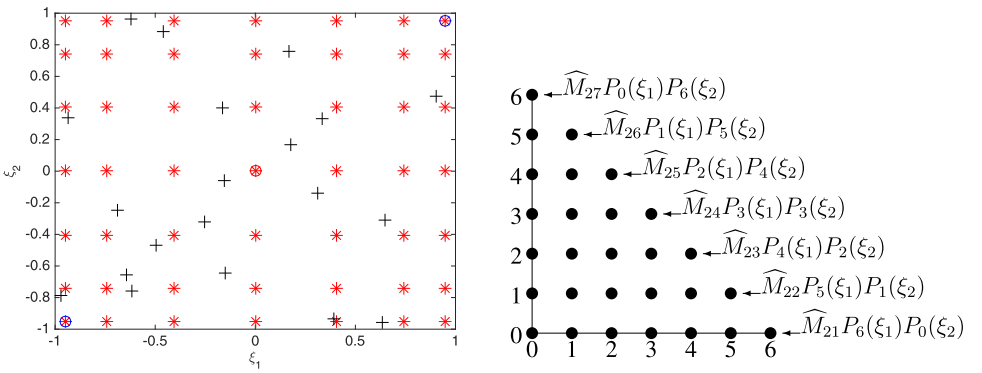

Figure 3. (left) Gauss Legendre quadrature (sample) points in the uncertain $\xi_1 - \xi_2$ space (red *); the center red circle shows to unperturbed run, while the blue circles correspond to the largest negative and positive perturbations; the black (+) signs show the settings of the 20 independent validation runs. (right) the polynomial degree in $\xi 1$ and $\xi 2$ retained in the series.

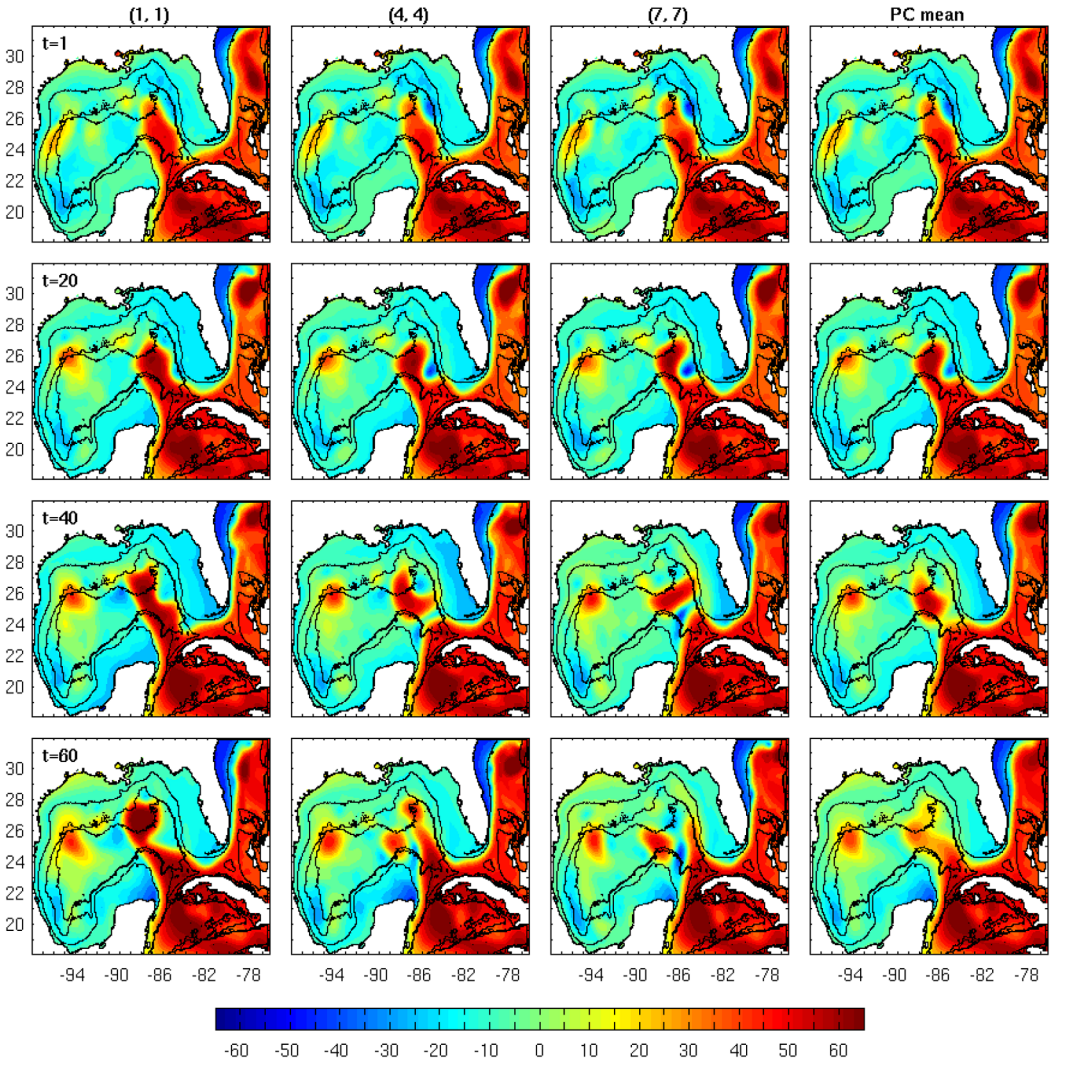

Figure 4. Time evolution of SSH realization (1,1) (first column) with weakest frontal eddy; of unperturbed realization (4,4) (second column) revealing a medium strength frontal eddy; and realization (7,7) (third column) with strongest frontal eddy. The fourth column shows the PC-ensemble mean of all 49 realizations, aka the 0-th mode of the PC-series. The times shown are in days since the start of the simulation, and SSH units are in cm.

occurs earlier for realizations associated with a stronger frontal eddy than for those associated with a weaker one. The ensemble mean of the SSH field reveals similar Loop Current dynamics: a northerly extended current cleaved by a frontal eddy, for the first 40 days; the 60-th day snapshot shows a diffused LC and LC eddy as a result of averaging different LC states. Figure 5 shows the Loop Current edge for all 49 realizations superimposed on the PC-mean SSH. At day 20 all realizations show an attached eddy, however, those with the strong frontal eddy show an imminent detachment about to occur while the one with the weak frontal eddy exhibits only the onset of LC necking. The day 40 snapshot shows realizations where the LC has already shed its eddy and has moved to a retracted position, while others are still in the middle of the shedding process. The mean SSH on day 40 shows a large detached eddy and a retracted LC. All realizations exhibit a LC eddy with the LC in retracted or retracting state. The diffused mean SSH in Figure 4 is mostly due to varying eddy locations among the ensemble members.

In order to ascertain whether the PC ensemble reflects realistic estimates of the uncertainty in SSH, we compare in Figure 6 the uncertainty in the location of the Loop Current edge [*Leben*, 2005] to its observed location as estimated from AVISO altimeter data. The AVISO estimate falls within the envelope of the possible states predicted by the PC ensemble throughout the 60 day period of the experiment. The EOF

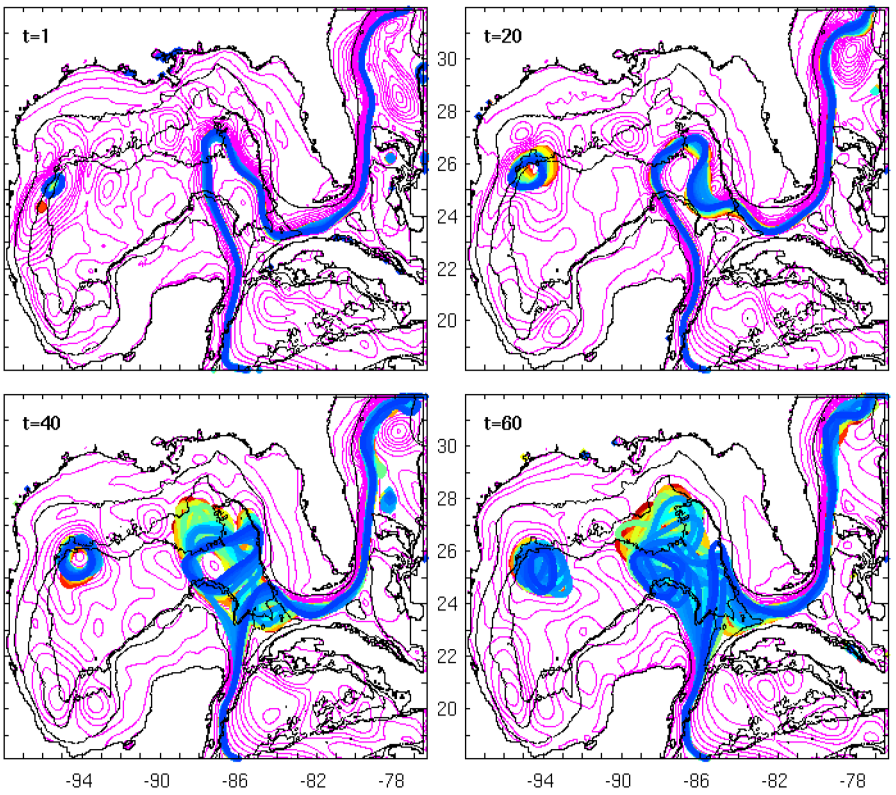

Figure 5. Loop Current evolution for all realizations. The thin magenta contours are the PC-mean of the SSH field, while the thick lines indicate the LC edge as defined by the 17 cm contour. The bluish thick lines are associated with the strong frontal eddy realizations whereas the reddish ones are associated with the weak frontal eddy.

decomposition and the PC analysis seem to have captured initial conditions perturbations that are consistent with observed oceanic states.

Figure 7 shows the temperature and salt profiles at the Deep Water Horizon (DWH) site for the unperturbed solution as well as for the most extreme perturbations. Here the EOF based perturbations show only a very small impact on the local temperature at early times and a slightly larger impact on the surface salt concentration. In both cases the perturbations impact is felt only indirectly, when perturbations emanating from the LC region have had time to propagate to the DWH site. This illustrates the large influence that the choice of initial perturbations plays in determining the ensuing uncertainty, and that their design must be informed by the intended objective of the uncertainty analysis. If the intended target is the to characterize the uncertainty around the DWH site then either a localized EOF analysis needs to be undertaken and/or additional sources of uncertainty must be included, such as wind stress forcing.

3.2. Surrogate Validation

We first attempt to establish the accuracy of the polynomial series before analyzing it for its statistical content. To this end we define the PC error as the difference between an actual model realization, $M(\boldsymbol{x}, t, \xi)$, and its PC representation, $M_P(\boldsymbol{x}, t, \xi)$:

$$\epsilon(\boldsymbol{x}, t, \xi) = M(\boldsymbol{x}, t, \xi) - M_P(\boldsymbol{x}, t, \xi) \tag{7}$$

An independent set of twenty randomly sampled realizations was performed in order to quantify the error in the surrogate. The locations ξ_v ($v=1, \ldots, V$) of the validation ensemble in the uncertain space are shown in black in Figure 3. The root mean square error provides an error measure across all realizations:

$$||\epsilon||_2^2 = \frac{1}{V}\sum_{v=1}^{V}[M(\boldsymbol{x}, t, \xi_v) - M_P(\boldsymbol{x}, t, \xi_v)]^2 \tag{8}$$

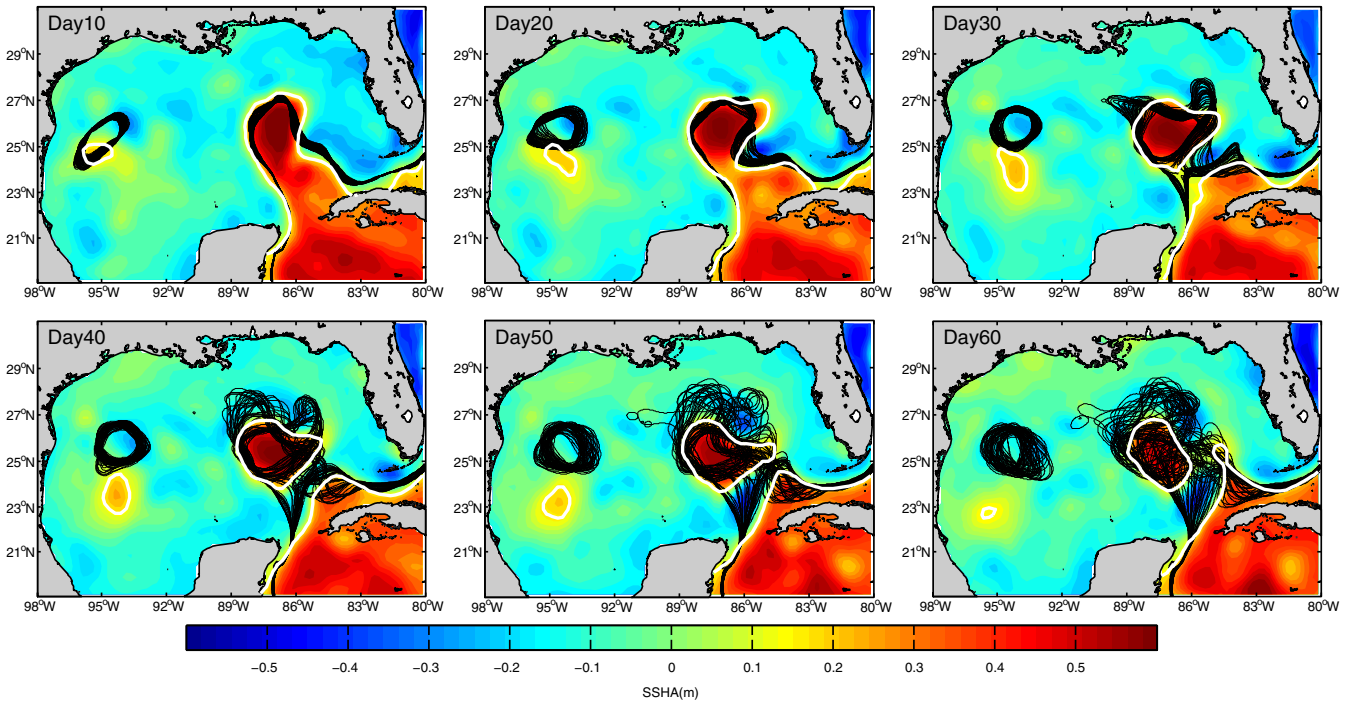

Figure 6. Time evolution of the SSH anomaly from AVISO altimetry data (color), with the Loop current edge, as defined by the 17 cm contour, in the PC ensemble (black lines) and in the AVISO data (white line).

Figure 8 (left) illustrates the evolution of the PC-error for the SSH field. The errors remain below the level of 2 cm for the first 20 days over the entire Gulf of Mexico. At day 40 the PC-error exhibits local maxima of about 6–10 cm in the general vicinity of the LC region and the LC pinch-off region. By day 60 the PC-error in SSH has reached levels of about 20 cm in the LC region and the maximum error levels have spread to a wider area. A similar pattern can be discerned on Figure 9 for a temperature section along 25N (which

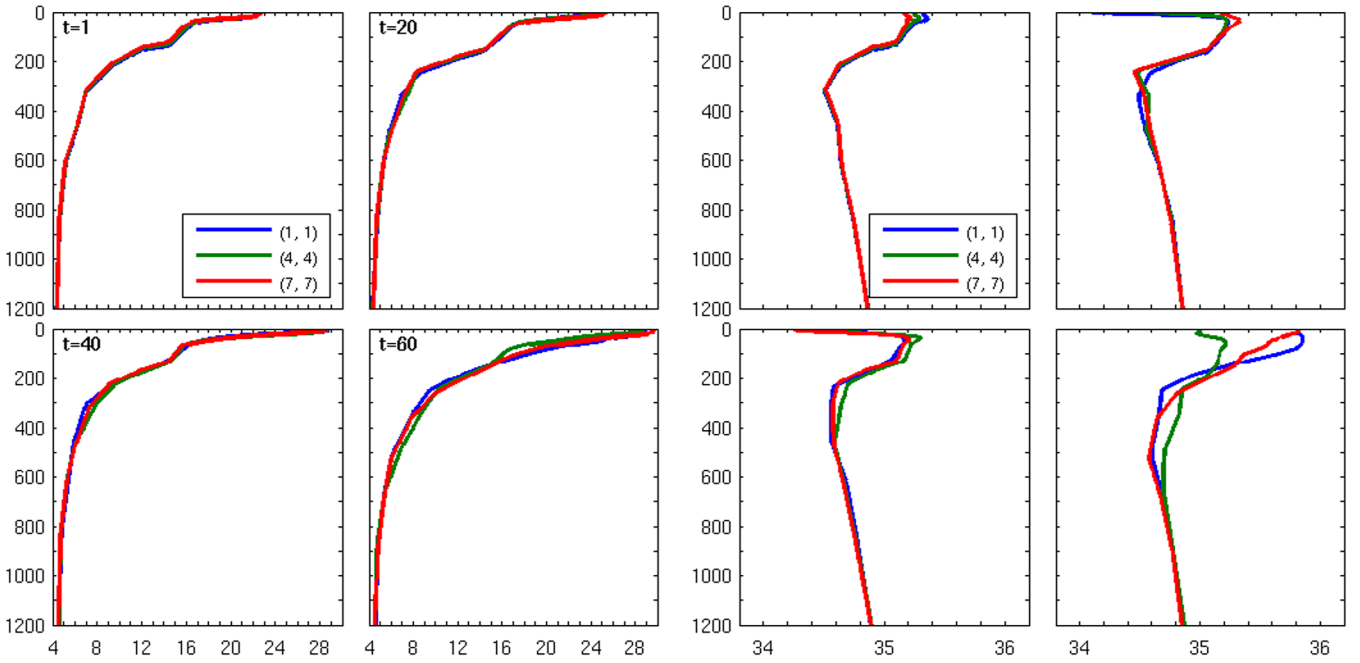

Figure 7. (left) Temperature and (right) salinity profiles at the DWH for the reference and extreme perturbations.

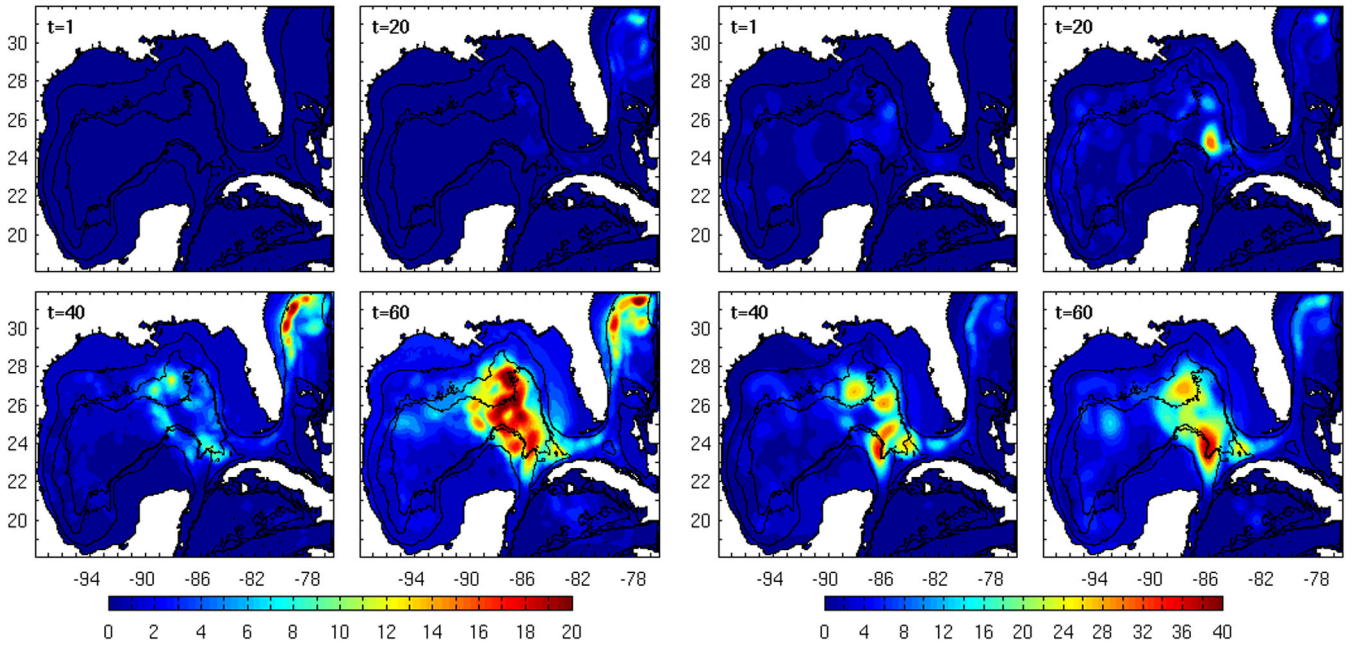

Figure 8. (left) Temporal evolution and spatial distribution of the PC error, $||\epsilon||$ (shown in cm), associated with SSH. The errors grow in time with their maxima located primarily in the dynamically active LC region. (right) Evolution of SSH stddev (in cm) as estimated from the PC-series; the areas of largest uncertainties are located in the LC region.

coincides with the general location of the frontal eddy). The errors are initially primarily located near the eastern and western edges of the Loop current. At day 20 the errors peak at less than 0.5°C, reach the 1.6°C range at day 40, and exceed 3°C locally by day 60. The areas of high errors expand with time as well and end-up occupying the entire depth range between 200 and 400 m depth. The evaluation of whether the error levels are tolerable to perform an uncertainty analysis will be discussed in section 3.3 when estimates of the variance in the model outputs are examined.

3.3. Statistical Moments of PC-Series

The mean of the model fields w.r.t. the uncertain inputs can be obtained by evaluating the integral:

$$E[M(\boldsymbol{x},t)]=\int M(\boldsymbol{x},t,\xi)\,\rho(\xi)\,\mathrm{d}\xi=\left\langle\sum_{n=0}^{P}\widehat{M}_n\psi_n,\psi_0\right\rangle=\widehat{M}_0||\psi_0||^2 \tag{9}$$

where the last equality follows from the orthogonality of the basis functions. If the basis functions are normalized so that $||\psi_0||=1$, the mean becomes simply the series zero-th coefficient. The PC-mean SSH field is shown in the last column of Figure 4.

The variance of the *M*-field can be shown to be:

$$var[M(\boldsymbol{x},t)]=E\left[\,(M-E[M])^2\,\right]=\sum_{n=1}^{P}\widehat{M}_n^2||\psi_n||^2. \tag{10}$$

Figure 8 (right) presents the evolution of the PC-based standard deviation as a measure of the uncertainty in SSH. The initial uncertainty is of the order of a few centimeters and its maximum seems to be associated with the frontal eddy strength. This maximum grows to about 28 cm by day 20 when the frontal eddy is cleaving the LC. Multiple maxima appear in the day 40 snapshots reflecting that some realizations have already shed their eddies while others still exhibit an extended LC; interestingly the largest maximum occurs in the southwestern corner of the LC edge.

Figure 9 shows the evolution of the temperature standard deviation at a vertical section along 25N. The initial conditions perturbations exhibit peaks at a depth of 100 m in the vicinity of the frontal eddy (to the east) and near the western edge of the LC with amplitudes of about 1.2 and 2.4°C, respectively. The eastern

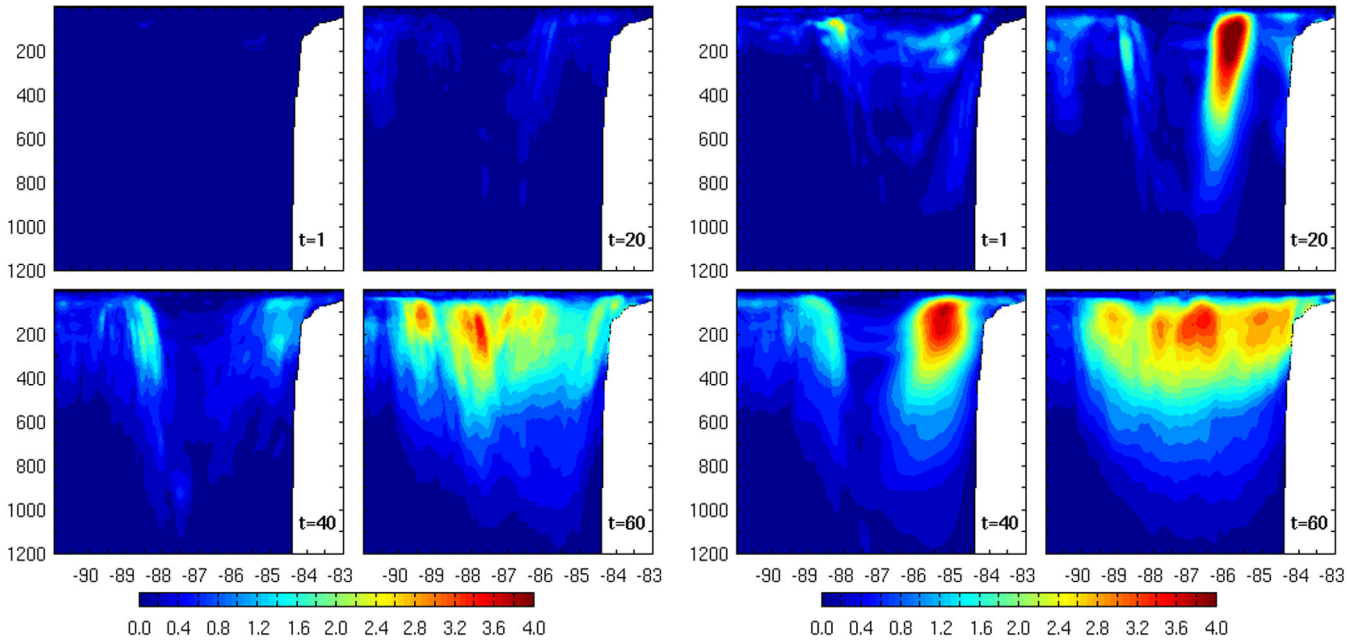

Figure 9. (left) The evolution of the PC-error associated with the temperature field along 25 N; the errors build up gradually with time and exceed 3°C by day 60 in the 200–400 m depth range. (right) The evolution of the temperature standard deviation with the uncertainty manifesting itself primarily on the easter side of the loop current. On day 60 the PC-error is about 100% of standard deviation.

peak grows rapidly to 4° C in the first 20 days and its depth range at day 20 extends from the near surface down to about 400 m; at day 40 the uncertainty spreads laterally to occupy a larger region (this large standard deviation of the temperature is probably caused by the frontal eddy occupying different positions in each realization). By day 60 the peak of the temperature standard deviation exceeds 2.4° C, and the region of high standard deviation has expanded to occupy the entire section between 90W and 85W from the surface down to a depth of 400 m. The western temperature uncertainty peak grows spatially at a lower rate while maintaining an amplitude of about 1.4° C.

The variance calculation requires summing the square of the coefficients in the series; hence premature truncation of the PC-series will result in an underestimation of the variance. It is thus essential that the PC-error remains small in order to gain confidence in the series estimates of the statistical moments. In the case of the SSH field for example, the PC-error at day 60 reaches 20 cm whereas the estimated standard deviation is 40 cm; the PC-error is thus about 50% of the standard deviation on that day. A similar trend can be seen for the temperature section where the error estimate remains low (compared to the standard deviation) for the first 40 days. By day 60 however, the peak errors are of comparable magnitude to the estimated standard deviation and hence there is little confidence in the day 60 results. Improvements in the surrogate's approximation properties requires a longer series than the one truncated at sixth degree polynomials, along with an increase in the ensemble size in order to determine the additional coefficients.

The relatively long record of AVISO altimetry data allows us to calculate the standard deviation of the SSH climatology, and subsequently to compare the variance of the present ensemble to that of the AVISO climatology. The AVISO standard deviation (Figure 10) exhibits a broad peak in the central portion of the region where the LC is active of about 35 cm. Figure 10 (right) shows the ratio of the forecast standard deviation to that of the climatology for the different days. The magenta lines show areas where the ratio exceeds unity, and where the spread in the ensemble is greater than the spread in the climatology. Variance ratios exceeding unity appear first in the LC pinch-off area (day 20) and manifest themselves later for the northern frontal LC region (between days 20 and 40). The localization in space and time of areas where the uncertainty in the model output is larger than climatological variability is a classical estimation of loss of predictability [*DelSole and Tippett*, 2007], because the model then is not able to bring more useful information than past observations. In our case, the fact that this limit is reached in the LC pinch-off region, which is associated with the most abrupt possible change in the Gulf dynamics in the form of an LCE detachment, defines the

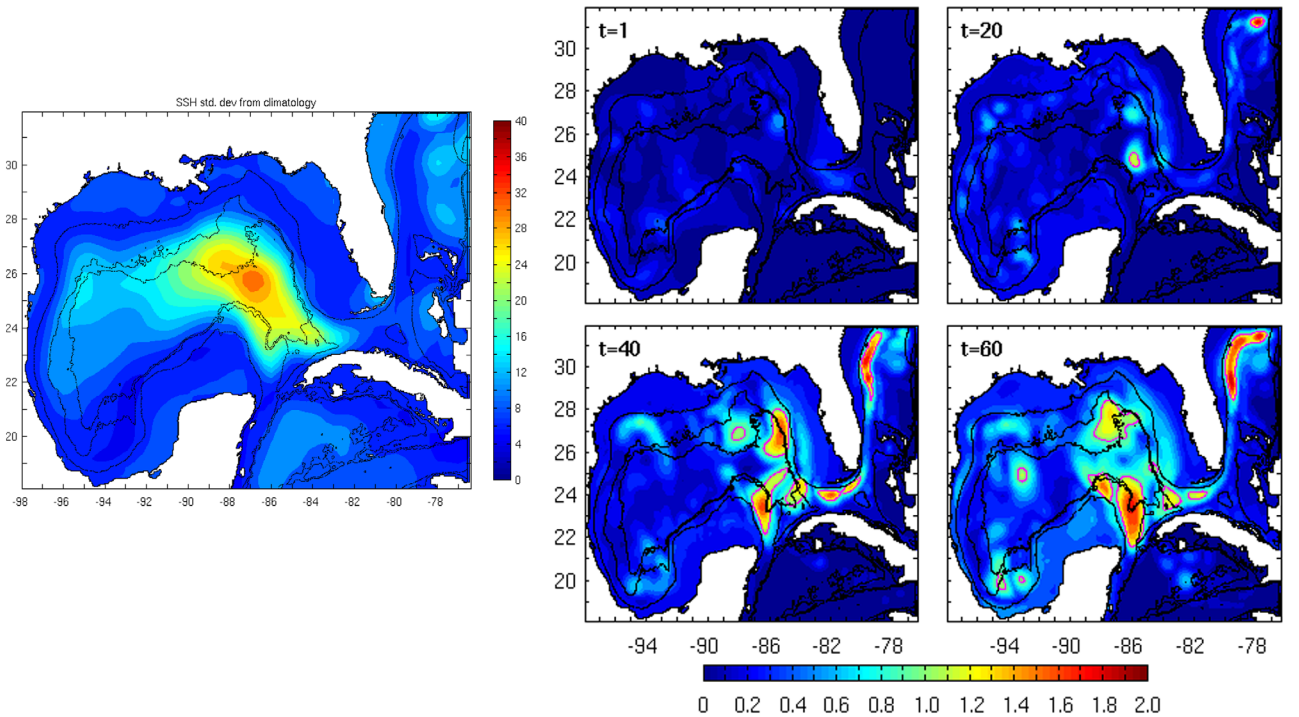

Figure 10. Variance Ratios: (left) The climatological SSH standard deviation as inferred from AVISO. (right) The evolution of the spatial distribution of the ratio of the forecast standard deviation to climatology standard deviation for SSH (from AVISO).

predictability limit of the LC system to be about 20 days. Information theory [*DelSole and Tippett*, 2007; *Liang*, 2011, 2014] provides more sophisticated alternative metrics to compare the forecast and climatological distributions and to assess the predictability of the forecast; we defer their presentation to future work.

The availability of the PC series permits the calculation of the covariance between different fields. Figure 11 shows the covariance between the SSH at the point marked by a white dot and the GOM SSH, and between that point SSH value and the temperature field along the vertical cross section. Note that the covariances peak in the neighborhood of the point SSH and decay fairly quickly away from it; furthermore the SSH-temperature covariance has a natural expression in the vertical. The covariance information can be useful for implementing a PC-based data assimilation system where the ensemble covariance matrix is estimated via the PC-series. This will be the subject of future work.

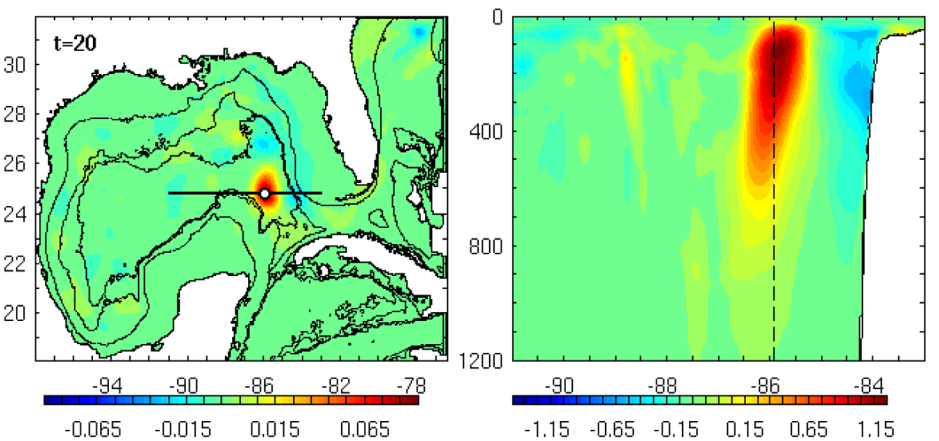

Figure 11. Covariances between one value of SSH (white dot circled in black) and the GoM SSH, and between the same SSH value and the vertical temperature along the longitude line indicated on the left figure. The SSH point location is marked on the section with dashed line. The units are m2 and m °C.

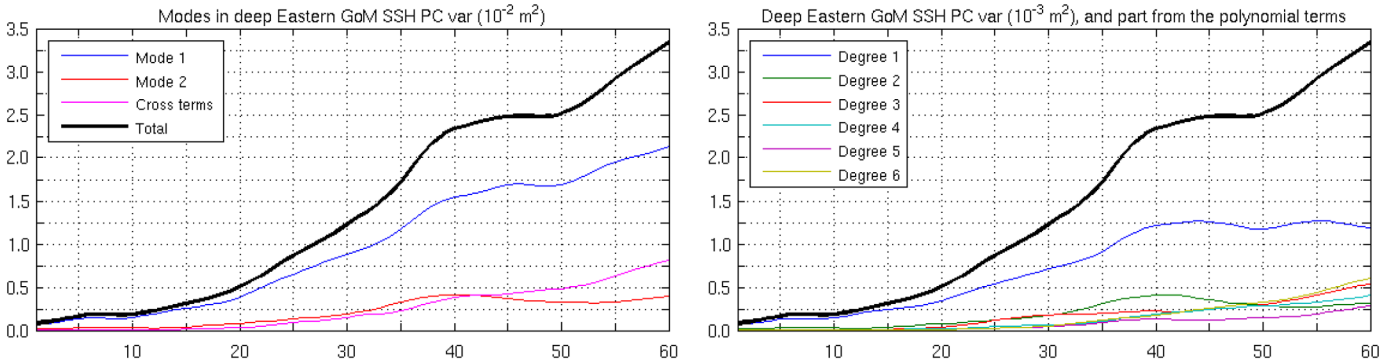

Figure 12. (left) Evolution of the SSH variance over the Deep Eastern part of the GoM (east of 90W and deeper than 2000 m) as contributed by the two modal perturbations and their interaction. (right) Contribution to the SSH variance over the deep Easter GoM by the different polynomial orders. The thick black lines shows the total variance whereas the thin black lines shows the contribution to the variance injected by the different polynomial orders.

Finally the orthogonality of the PC basis allows us to isolate the contribution of each term in the series to the total variance, and thus to assess the degree to which one uncertain variable contributes to the total variance, or whether the interaction of the two uncertainties leads to further growth in the model uncertainty. Figure 12 (left) shows that the SSH variance over the Deep Eastern part is dominated by the amplitude of the first modal perturbation which contributed about 3/4 and 2/3 of the total variance at day 20 and 40, respectively; its mean contribution over the first 30 days is 78%. The second perturbation mode contribution, on the other hand, starts very small, grows with time in tandem with that of the interaction terms and both provide the remaining variance (the second mode contributions are 16% on day 20, 18% on day 40 and averaging 16% over the first 30 days). Figure 12 (right) shows the contributions of the different (total) polynomial degrees to the total variance; it is thus a measure of the magnitude of the PC coefficients and consequently of the convergence of the PC series. The figures shows the magnitude of the highest (6-th degree) PC coefficients to be small but growing in time; by day 50 the 6-th degree polynomials produce a larger contribution to the variance than the other polynomial degrees except the first. This is another indication that the accuracy of the series has deteriorated and that statistics estimated beyond day 40 are not accurate.

4. Discussion and Summary

The present article has presented a PC-based approach to quantify the uncertainties in a HYCOM forecast of the circulation in the Gulf of Mexico caused by uncertainties in the model's initial conditions. The ingredients of this approach consist of first identifying variability modes of the system, second identifying the uncertain stochastic variables as the amplitudes of these modes and assigning them a probability density function, thirdly constructing surrogate series of specific model outputs using an ensemble of simulations, fourthly establishing the validity of the surrogate by monitoring its approximation errors, and finally analyzing the resulting surrogate series for statistical information.

In the present instance the variability modes were obtained through an EOF decomposition of a multivariate 14 day time series that specifically targeted the LC frontal dynamics; only two variability modes were retained in the present experiment. Analysis of the evolution of the LC eddy reveals that the two identified modes perturb the strength of the frontal eddy and, consequently, the evolution of the LC system. Comparison of the ensemble estimates of the LC location to that obtained from altimetry indicate that the perturbation reflect realistic uncertainties and that the PC approach has produced reasonable forecasts for the future location of the LC. Comparison to additional observations should be performed to ascertain whether other model outputs behave similarly. Furthermore, the approximation errors for the PC series were monitored: the 6-th degree polynomial series remained accurate for the first 20 days of the simulation for both SSH and temperature, remained acceptable between days 20 and 40 and started to deteriorate quickly after that. The peak errors were located in dynamically active regions, particularly in the vicinity of the LC detachment. Improvements to the series accuracy would require a higher polynomial truncation than sixth and would demand a larger quadrature ensemble. This extra cost however, has to be offset against the need to consider additional sources of uncertainty, such as adding additional perturbations to the initial conditions

or by considering wind forcing uncertainties for example. The examination of the variance contributed by each mode (Figure 12) shows that mode 1 alone contributes about 80% of the total SSH variance during the first 30 day period while the contributions of mode 2 alone remain small. This hints that adding higher EOFs modes with smaller initial variances to the initial condition perturbations would not alter the final variance estimates substantially, and that accounting for additional sources of uncertainties would be more useful.

Appendix A: Gauss Quadrature

Gauss quadrature rules [*Hildebrand*, 1987] are numerical approximations to integrals that have the form

$$\int_{-1}^{1} f(\xi)\rho(\xi)\mathrm{d}\xi=\sum_{i=1}^{n} f(\xi_i)\omega_i+\frac{f^{(2n)}(\xi_c)}{(2n)!}\int_{-1}^{1}\rho(\xi)[L_n(\xi)]^2\mathrm{d}\xi \tag{A1}$$

where ξ_i and ω_i are the n quadrature points and weights associated with the weight function $\rho(\xi)$ (assumed positive for $|\xi|<1$), $L_n(\xi)$ is the Lagrangian polynomial interpolant at the quadrature points, and $f^{(2n)}(\xi_c)$ represents the derivative of order $2n$ evaluated at a point within the interval of integration. The last term represents the quadrature error which vanishes if f happens to be a polynomial of degree $(2n-1)$ or less. Gaussian Quadrature relies heavily on the theory of orthogonal polynomials, i.e., those satisfying

$$(\psi_n,\psi_m)=\int_{-1}^{1}\psi_n(\xi)\psi_m(\xi)\rho(\xi)\mathrm{d}\xi=\begin{cases}0 & m\neq n\\ ||\psi_n||^2 & m=n\end{cases} \tag{A2}$$

which form a complete basis set for the space of square integrable functions. For example, when $\rho(\xi)=1$ the basis consists of Legendre polynomials, when $\rho(\xi)=(1-\xi)^{\alpha}(1+\xi)^{\beta}$ the basis consists of Jacobi polynomials, and when $\rho(\xi)=e^{-\frac{\xi^2}{2}}$ the basis consists of Hermite polynomials [*Xiu and Karniadakis*, 2002; *Le Maître and Knio*, 2010]. The n quadrature points are the roots of the n-th orthogonal polynomials with respect to the weight function $\rho(\xi)$, i.e., $\psi_n(\xi_i)=0$. The reader is referred to *Gautschi* [2004] for more information on Gauss quadrature and orthogonal polynomials and to *Ghanem and Spanos* [2003]; *Le Maître et al*. [2001]; *Xiu and Karniadakis* [2002]; *Le Maître and Knio* [2010] for their use in uncertainty quantification. The quadrature roots and weights for various polynomials are either tabulated [*Abramowitz and Stegun*, 1972] or can be computed using readily available software [*Gautschi*, 1994, 2005]. Table A1 lists the Gauss quadrature rules using 6 and 7 points for Legendre polynomials. In the one-dimensional case and considering a p-th order expansion, the Galerkin projection requires the computations of the norm of the basis functions whose maximal degree is $2p$; this can be handled exactly by using a quadrature rule with $n>(p+\frac{1}{2})$ points.

The two-dimensional tensorization of the Gauss quadrature formula in (ξ_1,ξ_2) space proceeds as follows:

$$\int_{-1}^{1}\left[\int_{-1}^{1} f(\xi_1,\xi_2)\rho(\xi_1)\mathrm{d}\xi_1\right]\rho(\xi_2)\mathrm{d}\xi_2\approx\int_{-1}^{1}\left[\sum_{i=1}^{n} f(\xi_{1,i},\xi_2)\omega_i\right]\rho(\xi_2)\mathrm{d}\xi_2 \tag{A3}$$

$$\approx\sum_{j=1}^{n}\left[\sum_{i=1}^{n} f(\xi_{1,i},\xi_{2,j})\omega_i\right]\omega_j \tag{A4}$$

$$=\sum_{j=1}^{n}\sum_{i=1}^{n} f(\xi_{1,i},\xi_{2,j})\omega_i\omega_j \tag{A5}$$

Table A1. Table of Gauss Quadrature Roots and Weights Using 6 and 7 Points[a]

n=6		n=7	
ξ_i	ω_i	ξ_i	ω_i
± 0.932469514203152	0.171324492379171	± 0.949107912342759	0.129484966168869
± 0.661209386466265	0.360761573048138	± 0.741531185599394	0.279705391489276
± 0.238619186083197	0.467913934572692	± 0.405845151377397	0.381830050505119
		0.000000000000000	0.417959183673469

[a]The roots are symmetric with respect to 0. Notice that the roots cluster near the edges of the interval as n increases.

The two-dimensional layout of the quadrature roots is shown in Figure 3. Dimensional tensorization leads to an exponential growth in the number of function evaluations as the number of dimensions increases. Alternative "sparse" integration rules [*Smolyak*, 1963; *Gerstner and Griebel*, 1998] and adaptive sparse pseudospectral series [*Conrad and Marzouk*, 2013; *Winokur et al*., 2013] were developed to mitigate this growth.

Acknowledgments
We would like to thank the two anonymous reviewers whose comments were extremely helpful in improving the manuscript. This research was made possible in part by a grant from BP/The Gulf of Mexico Research Initiative to the CARTHE and DEEP-C Consortia, and by the Office of Naval Research, Award N00014-101-0498. O. M. Knio was supported in part by the US Department of Energy (DOE), Office of Science, Office of Advanced Scientific Computing Research, under Award Number DE-SC0008789. M. Le Hénaff received partial support for this work from the NOAA Quantitative Observing System Assessment Program (QOSAP, grant NA15OAR4320064) and the base funds of the NOAA Atlantic Oceanographic and Meteorological Laboratory. The altimeter products were produced by SSALTO/DUACS and distributed by AVISO (http://www.aviso.altimetry.fr/duacs/), with support from the Centre National dEtudes Spatiales (CNES). The model outputs used in the present study are available on GRIIDC website (https://data.gulfresearchinitiative.org/).

References

Abramowitz, M., and I. E. Stegun (1972), *Handbook of Mathematical Functions*, U.S. Dep. of Commer., Natl. Bur. of Stand., Washington, D. C.
Bleck, R. (2002), An oceanic general circulation model framed in hybrid isopycnic cartesian coordinates, *Ocean Modell.*, *4*(2), 55–88, doi:10.1016/S1463-5003(01)00012-9.
Chassignet, E. P., H. E. Hurlburt, O. M. Smedstad, G. R. Halliwell, P. J. Hogan, A. J. Wallcraft, R. Baraille, and R. Bleck (2007), The HYCOM (HYbrid Coordinate Ocean Model) data assimilative system, *J. Mar. Syst.*, *65*(1-4), 60–83, doi:10.1016/j.jmarsys.2005.09.016.
Curcic, M., S. S. Chen, and T. M. Özgökmen (2016), Hurricane-induced ocean waves and stokes drift and their impacts on surface transport and dispersion in the Gulf of Mexico, *Geophys. Res. Lett.*, *43*, 2773–2781, doi:10.1002/2015GL067619, 2015GL067619.
DelSole, T., and M. K. Tippett (2007), Predictability: Recent insights from information theory, *Rev. Geophys.*, *45*, RG4002, doi:10.1029/2006RG000202.
Gautschi, W. (1994), Algorithm 726: Orthopol—A package of routines for generating orthogonal polynomials and Gauss-type quadrature rules, *ACM Trans. Math. Software*, *20*(1), 21–62, doi:10.1145/174603.174605.
Gautschi, W. (2004), *Orthogonal Polynomials Computation and Approximation*, Numer. Math. and Sci. Comput., Oxford Univ. Press, Oxford, U. K.
Gautschi, W. (2005), Orthogonal polynomials (in matlab), *J. Comput. Appl. Math.*, *178*(1–2), 215–234, doi:10.1016/j.cam.2004.03.029.
Gerstner, T., and M. Griebel (1998), *Numerical integration using sparse grids, Numer. Algorithms*, *18*, 209–232, doi:10.1023/A:1019129717644.
Ghanem, R., and P. Spanos (2003), *Stochastic Finite Elements: A Spectral Approach, Revised Edition*, 2nd ed., Dover, Mineola, N. Y.
Hildebrand, F. B. (1987), *Introduction to Numerical Analysis*, 2nd ed., Dover, N. Y.
Hodur, R. (1997), The naval research laboratory's coupled ocean/atmosphere mesoscale prediction system (coamps), *Mon. Weather Rev.*, *125*(7), 1414–1430, doi:10.1175/1520-0493(1997)125<1414:TNRLSC>2.0.CO;2.
Iskandarani, M., S. Wang, A. Srinivasan, W. C. Thacker, J. Winokur, and O. M. Knio (2016), An overview of uncertainty quantification techniques with application to oceanic and oil-spill simulations, *J. Geophys. Res. Oceans*, *121*, 2789–2808, doi:10.1002/2015JC011366.
Kantha, L. (2014), Empirical models of the loop current eddy detachment/separation time in the Gulf of Mexico, *J. Waterw. Port Coastal Ocean Eng.*, *140*(3), 04014001–1, doi:10.1061/(ASCE)WW.1943-5460.0000220.
Le Hénaff, M., V. H. Kourafalou, C. B. Paris, J. Helgers, Z. M. Aman, P. J. Hogan, and A. Srinivasan (2012), Surface evolution of the deepwater horizon oil spill patch: Combined effects of circulation and wind-induced drift, *Environ. Sci. Technol.*, *46*(13), 7267–7273, doi:10.1021/es301570w.
Leben, R. R. (2005), Altimeter derived loop current metrics, in *Circulation in the Gulf of Mexico: Observations and Models, Geophys. Monogr. Ser.*, vol. 161, edited by W. Sturges and A. Lugo-Fernandez, pp. 181–201, AGU, Washington, D. C.
Le Maître, O., and O. Knio (2010), *Spectral Methods for Uncertainty Quantification With Applications to Computational Fluid Dynamics*, Scientific Computation, Springer, N. Y.
Le Maître, O., O. Knio, H. Najm, and R. Ghanem (2001), A stochastic projection method for fluid flow. I. Basic formulation, *J. Comput. Phys.*, *173*, 481–511.
Le Maître, O., M. Reagan, H. Najm, R. Ghanem, and O. Knio (2002), A stochastic projection method for fluid flow. II. Random process, *J. Comput. Phys.*, *181*, 9–44, doi:10.1006/jcph.2002.7104.
Liang, X. S. (2011), Uncertainty generation in deterministic flows: Theory and application with an atmospheric jet stream model, *Dyn. Atmos. Oceans*, *52*(1–2), 51–79, doi:10.1016/j.dynatmoce.2011.03.003.
Liang, X. S. (2014), Entropy evolution and uncertainty estimation with dynamical systems, *Entropy*, *16*, 3605–3634, doi:10.3390/e16073605.
Najm, H. (2009), Uncertainty quantification and polynomial chaos techniques in computational fluid dynamics, *Annu. Rev. Fluid Mech.*, *41*, 35–52.
Nobile, R. T., and C. Webster (2008), A sparse grid stochastic collocation method for partial differential equations with random input data, *SIAM J. Numer. Anal.*, *46*(5), 2309–2345, doi:10.1137/060663660.
Oey, L.-Y., T. Ezer, and H.-C. Lee (2005), Loop current, rings and related circulation in the Gulf of Mexico: A review of numerical models and future challenges, in *Circulation in the Gulf of Mexico: Observations and Models, Geophys. Monogr. Ser.*, vol. 161, edited by W. Sturges and A. Lugo-Fernandez, pp. 31–56, AGU, Washington, D. C.
Patrick R., Conrad, and Y. M. Marzouk (2013), Adaptive Smolyak Pseudospectral Approximations, *SIAM Journal on Scientific Computing*, *356*, pp. A2643–A2670, doi:10.1137/120890715.
Reed, M., O. Johansen, P. J. Brandvik, P. Daling, A. Lewis, R. Fiocco, D. Mackay, and R. Prentki (1999), Oil spill modeling towards the close of the 20th century: Overview of the state of the art, *Spill Sci. Technol. Bull.*, *5*(1), 3–16, doi:10.1016/S1353-2561(98)00029-2.
Sapsis, T. P., and P. F. Lermusiaux (2009), Dynamically orthogonal field equations for continuous stochastic dynamical systems, *Physica D*, *238*, 2347–2360, doi:10.1016/j.physd.2009.09.017.
Smolyak, S. (1963), Quadrature and interpolation formulas for tensor products of certain classes of functions, *Dokl. Akad. Nauk SSSR*, *4*, 240–243.
Sraj, I., M. Iskandarani, W. C. Thacker, A. Srinivasan, and O. M. Knio (2014), Drag parameter estimation using gradients and hessian from a polynomial chaos model surrogate, *Mon. Weather Rev.*, *142*(2), 933–941, doi:10.1175/MWR-D-13-00087.1.
Thacker, W. C., M. Iskandarani, R. C. Gonçalves, A. Srinivasan, and O. M. Knio (2015), Pragmatic aspects of uncertainty propagation: A conceptual review, *Ocean Modell.*, *95*, 25–36, doi:10.1016/j.ocemod.2015.09.001.
Ueckermann, M. P., P. F. Lermusiaux, and T. P. Sapsis (2013), Numerical schemes for dynamically orthogonal equations of stochastic fluid and ocean flows, *J. Comput. Phys.*, *233*, 272–294, doi:10.1016/j.jcp.2012.08.041.
Winokur, J., P. Conrad, I. Sraj, O. M. KNio, A. Srinivasan, W. C. Thacker, Y. Marzouk, and M. Iskandarani (2013), A priori testing of sparse adaptive polynomial chaos expansions using an ocean general circulation model database, *Comput. Geosci.*, *17*(6), 899–911, doi:10.1007/s10596-013-9361-3.
Xiu, D., and J. Hesthaven (2005), High-order collocation methods for differential equations with random inputs, *SIAM J. Sci. Comput.*, *27*(3), 1118–1139, doi:10.1137/040615201.
Xiu, D., and G. Karniadakis (2002), The Wiener-Askey Polynomial Chaos for stochastic differential equations, *SIAM J. Sci. Comput.*, *24*, 619–644.